

## RESEARCH ARTICLE

WILEY

# Identifying the flap side-edge noise contribution of a wind turbine blade section with an adaptive trailing edge

A. Suryadi<sup>1</sup>  | C. Jätz<sup>2</sup> | J.R. Seume<sup>2</sup> | M. Herr<sup>1</sup>

<sup>1</sup>German Aerospace Center, Institute of Aerodynamics and Flow Technology, Lilienthalplatz 7, Braunschweig, 38108, Germany

<sup>2</sup>Institute of Turbomachinery and Fluid Dynamics, ForWind and Leibniz University Hannover, An der Universität 1, Garbsen, 30823, Germany

## Correspondence

A. Suryadi, German Aerospace Center, Institute of Aerodynamics and Flow Technology, Lilienthalplatz 7, Braunschweig 38108, Germany.  
Email: [alexandre.suryadi@dlr.de](mailto:alexandre.suryadi@dlr.de)

## Funding information

German Ministry for Economic Affairs and Energy

## Abstract

Active trailing-edge technology is a promising application for localized load alleviation of large-diameter wind turbine rotors, accomplished using one or more control surfaces in the rotor blade's outer region. This work focuses on identifying noise contributions from the flap side-edge and the trailing edge in a laboratory condition. Measurements were conducted in the Acoustic Wind Tunnel Braunschweig (AWB) at the German Aerospace Center's (DLR) Braunschweig site. The small-scale model has a span of 1,200 mm and a chord length of 300 mm. The control surface, a plain flap, has a span of 400 mm and a chord length of 90 mm. Far-field noise was measured using a phased-microphone array for various flow speeds, angles of attack, and flap deflection angles. Due to the size of the model and assumed closeness of the sound sources, two noise reduction *addons* were installed interchangeably: trailing-edge brush and flap side-edge porous foam for sound source identification. Analysis of the far-field noise reveals that, while changes to the flap deflection angle alter the far-field noise spectra, the trailing-edge noise remains the predominant noise source at deflection angles  $-5^\circ$  and  $5^\circ$ . No additional noise level was observed from the flap side edge within the measurable frequency range at these angles. The flap side-edge noise has an increased role for frequency larger than 2 kHz for the larger flap deflection angles of  $-10^\circ$  and  $10^\circ$ .

## 1 | INTRODUCTION

The trend in the wind energy industry is towards larger rotor blades to produce more electricity from a single turbine. Larger rotors will experience stronger and more dynamic loads due to the fluctuating and heterogeneous wind field. Hence, there is an interest in locally distributed aerodynamic control systems. Pitch control is one strategy of load alleviation to maintain the blade's angle of attack, so that its load can be kept, on average, constant. With a larger blade, local changes to the load are preferable. One strategy uses active trailing edges; such devices can be a flap or an aileron. Either way, it modifies the lift coefficient by changing the overall shape of the rear part of the profile equivalent to a change in the camber of the overall profile.

Load alleviation is studied in the framework of project *SmartBlades 2.0*, which has the overall goal of demonstrating the practical applications of technologies for rotor blade control and validating suitable innovative numerical tools and manufacturing methods. One of the technologies studied in the project is load alleviation using an active trailing edge. This is presently accomplished using a plain flap on the outboard section ( $0.825 \leq R/R \leq 0.9$ ) of the rotor blade from the conceptual wind turbine IWES IWT-7.5-164,<sup>1</sup> which has a blade length of  $R = 80$  m. The present plain flap installation means that when active, the trailing edge is no longer a continuous line and a new edge is exposed from the flap's side. The newly exposed edges have the potential to radiate noise.

Flap side-edge noise has been covered extensively in the aeronautical industry,<sup>2-12</sup> whereas in the wind energy industry, the study focuses on the implementation and the aerodynamic effect of flap on wind turbine rotor blades.<sup>13-17</sup> In aeronautics, the flap is implemented differently than in the wind energy industry, namely, in the types of flap used, Fowler flap in aeronautics and plain flap in wind energy, and in the degree of flap deflection,  $\delta_f > 20^\circ$  in aeronautics<sup>9,18</sup> and  $|\delta_f| \leq 10^\circ$  in wind energy.<sup>15</sup> To the authors' knowledge, the noise radiation from the flap side-edge of a rotor blade has not been extensively explored. A few reasons for this state of the art are as follows: (i) The desired implementation is one that maintains a continuous trailing edge, and (ii) the flap deflection angle is small enough that flap side-edge noise is assumed negligible. The objective of this paper is to identify the contributions between the flap side-edge noise and trailing-edge noise for a deflected flap.

In this study, a small-scale test was conducted in the Acoustic Wind Tunnel Braunschweig located at the German Aerospace Center's (DLR) Braunschweig site to measure and rank the flap side-edge noise compared to the trailing-edge noise. A segment of the rotor blade, shaped as a DU08-W-180 profile, is scaled down as a 1,200 mm span and a 300 mm chord wind tunnel model. The model's shape and chord length are constant. The plain flap has a 400 mm span and a 90 mm chord, capable of being deflected negatively (upwards, towards the suction side) and positively (downwards, towards the pressure side). As a comparison, the small-scale wind tunnel model has a chord-based Reynolds number of  $0.95 \times 10^6$ , whereas a similar section in the full-scale rotor has  $12.6 \times 10^6$ .

The paper is structured as follows: First, the experimental setup is detailed, followed by an explanation of the identification of sound sources using noise reduction materials. The results are presented and discussed in the two following sections, and finally, a conclusion from the study is drawn.

## 2 | EXPERIMENTAL SETUP

### 2.1 | Wind tunnel facility

The Acoustic Wind Tunnel Braunschweig (AWB) is a Göttingen type, open section, acoustically insulated wind tunnel. It is capable of producing a maximum wind speed of 65 m/s with 0.3% turbulence intensity.<sup>19</sup> The freestream is introduced into the open section from a 0.8 m wide and 1.2 m high nozzle.

The wind tunnel's test section and the blade model installed within are shown in Figure 1. A phased-microphone array with 96, 1/2-inch LinearX microphones was placed approximately 1 m away from the trailing edge to measure the blade model's self-noise. The distance was selected to avoid the interaction between the microphones and the wind tunnel's shear layer. The microphones on the phased array are positioned inside a 1 m diameter circle. Two synchronized 48-channel (16-bit, 200 kHz maximum sampling rate/channel) high precision GBM Viper data acquisition systems were used to record the far-field noise signal. The measurement has a sampling rate 65 kHz and a sampling time of 20 s. The microphones' output was filtered with a high-pass filter with a cut-off frequency of 500 Hz.

The phased-microphone array had been calibrated using a loudspeaker producing white noise with a dynamic range of  $700 \text{ Hz} < f < 20,000 \text{ Hz}$  and non-intrusively using a laser-generated sound source.<sup>20</sup> The phased-microphone array showed a reliable frequency range of  $800 \text{ Hz} < f < 10,000 \text{ Hz}$ , with the upper frequency limited by the dispersion effect from the shear layer. The reliability of the phased-microphone array with the installed support structure will be further discussed in Section 5.2.

Noise mapping was performed using the CLEAN-SC algorithm, which allows for separating different noise sources by defining specific regions of interest on the model.<sup>21</sup> The algorithm provides a margin of approximately  $\pm 2 \text{ dB}$  within a 95% confidence interval. The spatial distribution of



**FIGURE 1** The blade section model (1), with a plain flap (2), and the phased-microphone array (3), inside the AWB test section. Also shown are the wind tunnel nozzle (4) and collector (5)

the microphones and their distances to the trailing edge means that the resulting sound pressure is an average covering an approximately  $53^\circ$  arc of the noise directivity. The final sound pressure level spectra are referenced to an observer 1 m away from the trailing edge of the model. Measurements were conducted with the phased-microphone array alternately facing the blade model's suction and pressure sides, and it was found that there is no unexpected difference from either side, so the upcoming analysis will present only the suction side.

## 2.2 | Blade section model

The blade section model with DU08-W-180 profile was installed vertically in the wind tunnel section, as shown in Figure 1. The model has a span of 1,200 mm and a chord length of 300 mm. The plain flap was installed in the mid-span section of the model. The flap's span is 400 mm, and its chord length is 90 mm; see also Figure 2. A motor is attached to the outside of the model to drive the flap. During the measurements, the flap angle is fixed, and the flap is only driven in-between measurements.

By design, wind turbine rotors have a thick blunt trailing edge. The chord-length based scaling down of the model results in a trailing edge thickness of 2 mm leading to bluntness noise in the laboratory scale. Hence, the trailing edge is further reduced to 0.3 mm, akin to a sharp trailing edge.

For motion with minimal friction, the gap between the flap side edge and the model's side edge is approximately 0.2 mm. This gap is left untreated. The gap in the span-wise direction between the flap and the model is sealed using aluminum tape, creating a smooth and continuous transition between both parts and preventing a cross-flow from the pressure side to the suction side, eliminating potential acoustic noise source.

The blade section model is equipped with two sets of 25 static pressure ports. The first set is along the mid-span for monitoring the pressure coefficients when the flap is deflected and the second set is 400 mm away from the mid-span for monitoring the reference, zero-flap-deflection pressure coefficients. The pressure distribution was measured using DTI Initium electronic pressure scanning data acquisition system with a sampling time of 15 s. The boundary layer was tripped using a 0.205 mm high zig-zag trip on the suction side at the  $x/c = 0.05$  and on the pressure side at the  $x/c = 0.10$  to emulate the high Reynolds number transition location.

## 2.3 | Experimental parameters

The angular parameters shown in Table 1 were measured in the wind tunnel at windspeeds of  $U_0 = 40, 50, \text{ and } 60$  m/s. The angle of attack  $\alpha_g$  signifies the geometric angle as set in the wind tunnel, i.e., the angle relative to the center plane of the wind tunnel. Prior to the acoustic measurements, the pressure coefficient over a range of  $\alpha_g$ s and zero flap deflection angle were measured. The equivalent aerodynamic angle of attack,  $\alpha_a$ , was determined by comparing the measured pressure coefficient distributions with that calculated using XFOIL.<sup>22</sup>

For  $\alpha_g = 13^\circ$ , the flap deflection angles  $\delta_f$  are limited because the combination of the large angle of attack, and positive flap deflection causes the wake to be deflected outside of the flow collector region.

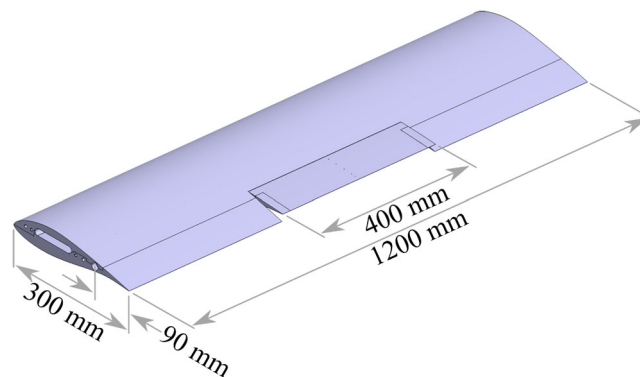


**FIGURE 2** The blade section model DU08-W-180 with flap set at  $\delta_f = -10^\circ$

**TABLE 1** Angle of attack  $\alpha_g$ ,  $\alpha_a$ , and flap deflection angle  $\delta_f$

$\alpha_g, ^\circ$	$\alpha_a, ^\circ$	$\delta_f, ^\circ$
5	0	-10, -5, -4, ... 4, 5, 10
7	3	-10, -5, -4, ... 4, 5, 10
13	6	-10, -5, -4, ... 0

### 3 | NUMERICAL SETUP

Steady RANS simulations provide a detailed insight into the flow field and are the input for the computational aeroacoustic analysis. The discussion on the computational aeroacoustic results is outside the scope of this paper and will be left for another publication. The setup of the RANS simulation is provided here to evaluate the flap side-edge vortex dynamics as it pertains to the discussion of the experimental results.

Due to symmetry, the size of the model, and the required high mesh resolution, the numerical domain comprises only a side-edge and extends 150 mm span-wise in both directions. The far field extends to 100 chord lengths. The mesh is block structured. The topology was carefully designed so that the cells between all blocks in the side-edge region match conformally. This eliminates the need for an interpolating interface, eliminating spurious errors in the region of interest. The initial cell height at the blade surface was chosen to achieve a  $y^+$  value of less than 1. This allows the application of low-Reynolds number turbulence models for a more accurate representation of the boundary layer. The growth ratio in wall-normal direction is 1.1. The cell resolution in the side-edge region was increased according to the requirements for the aeroacoustic analysis. Overall, the mesh contains about  $30 \times 10^6$  cells.

The simulations were carried out using the coupled implicit solver with a second-order discretization in Star CCM+. For closure of the RANS equations, the  $k-\omega$  SST turbulence model was selected as this model provides the required flow field quantities for the subsequent aeroacoustic analysis. In order to capture the forced transition by the applied tripping in the wind tunnel, a turbulent suppression approach was selected. Here, the turbulence model is deactivated upstream of the tripping location, resulting in a laminar flow. Downstream of the tripping location, a turbulent boundary layer develops.

The convergence of the simulations was verified by the decrease of the average and maximum residuals. Additionally, lift and drag coefficients were monitored as they converged to constant values.

### 4 | NOISE REDUCTION TECHNOLOGIES

Noise mitigating add-ons were used to inhibit selective noise radiation and to identify the noise source from a blade section of the present scale. For example, to identify the contribution of the flap side-edge noise, noise-reducing brush was added to the trailing edge. Conversely, to identify the contribution of the trailing-edge noise, the flap side-edge is substituted with a porous copy.

#### 4.1 | Trailing-edge brush

The trailing-edge brush<sup>23</sup> consists of elastic needles that are 0.4 mm in diameter. The brush is one layer thick and with a density of 250 needles/m along the span and a length of 60 mm. It was installed on the trailing edge's pressure side using a double-sided adhesive tape. Further structural support is provided by an aluminum tape, which also allows for a smooth transition of the boundary layer from the model's surface to the brush. The installed trailing-edge brush is shown in Figure 3A.

#### 4.2 | Porous side-edges

Two porous copies of the flap side-edges were manufactured using an electrical discharge machining process. This process allows for shaping the porous foam to the shape of the flap side-edge. These substitutes, when installed, will provide a porous side-edge with a depth of 20 mm. The porous materials are PA 80-110 and PA 120-150, which were supplied by Exxentis AG. The properties of the porous materials are provided in Table 2, and the two materials are shown in Figure 3B,C. The porosity, the ratio of open volume to the total volume, the specific resistance, and the pressure loss of a flow passing the material per unit velocity were measured by the Institute for Materials, TU Braunschweig. These materials were extensively investigated for trailing-edge noise reduction.<sup>24,25</sup>

### 5 | RESULTS

#### 5.1 | Pressure coefficients

The measured pressure coefficients are shown in Figure 4 for all measured angles of attack. For brevity only  $\delta_f = -10^\circ, -5^\circ, 0^\circ, 5^\circ,$  and  $10^\circ$  are shown for the pressure coefficients and the sound pressure levels. The margin of error for the measured pressure coefficient is  $\pm 0.026$  within a 95% confidence interval.

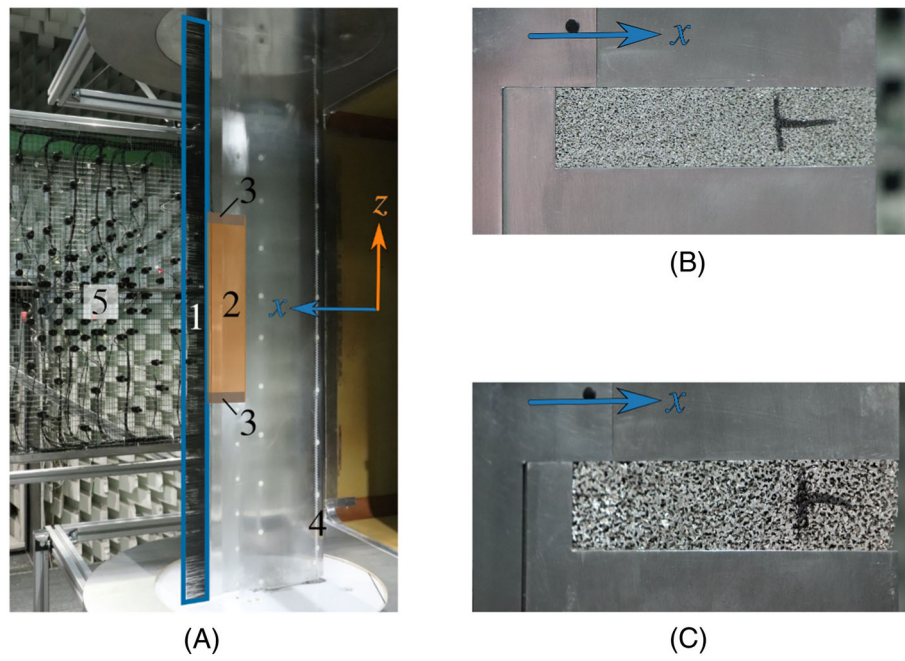


**FIGURE 3** (A) The blade section model viewed from the pressure side with the trailing-edge brush (1), the flap (2), the exchangeable flap side-edges (3), the boundary layer tripping (4), and the phased-microphone array (5). Porous flap side-edges, (B) PA80-110 and (C) PA120-150, viewed from the suction side of the blade section model

**TABLE 2** Porous material properties

Specimen	Nominal pore size [ $\mu\text{m}$ ]	Porosity [%]	Specific resistance [ $\text{Ns}/\text{m}^3$ ]
PA 80-110	80-110	56	540
PA 120-150	120-150	57	245

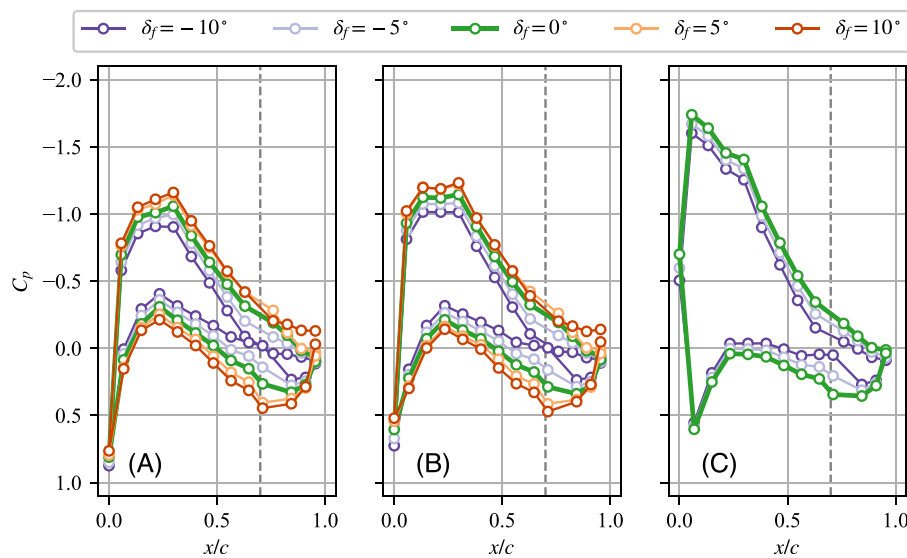


**FIGURE 4** Experimental pressure coefficients at  $\delta_f = 0^\circ$  and  $|\delta_f| = 5^\circ$  and  $10^\circ$ , (A)  $\alpha_g = 5^\circ$ , (B)  $\alpha_g = 7^\circ$ , and (C)  $\alpha_g = 13^\circ$ . The flap starts at  $x/c = 0.7$  as depicted by the vertical gray dashed line

## 5.2 | Relevant frequency range

The exterior noise that is sourced from anything other than the model's self-noise was measured with the same tools and the relevant measurement parameters without the blade section model installed to identify the meaningful frequency range. For this purpose, the region of interest defined in CLEAN-SC for the analysis of trailing-edge noise is an area with a span width of  $b_g = 0.7$  m and streamwise length of  $c_g = 0.2$  m. For the analysis of exterior noise, the region of interest encompasses the full span of the blade section model,  $b_g = 1.2$  m and from the AWB nozzle to 1.2 m downstream.

The sound maps of the exterior noise for selected one-third octave center frequencies are shown in Figure 5A with the position where the blade model would be depicted as the dashed line, and in Figure 5B for the trailing-edge noise with the blade model depicted as the solid line. The sound maps' red line highlights the sound contour where  $\max(L_{p,1/3}) - 3$  dB. The trailing edge is located at  $x = 0.55$  m, and at  $x = 0.8$  m is the location of the edge of the top and bottom support walls (see Figure 1). The sound maps in Figure 5A show that the support walls' edges radiate sound that is louder than the trailing-edge noise at  $f_c = 5,000$  Hz, and it remains louder for center frequencies higher than 5,000 Hz. Despite this, the sound pressure levels at  $f_c > 5,000$  Hz scale well with the  $U_0^5$  trailing-edge noise, as shown in the next section, because of the decreasing acoustic wavelength. Hence, due to excess noise from the edges of the support walls, the figures involving sound pressure level will exclude the spectral level at  $f_c = 5,000$  Hz.

## 5.3 | Reference trailing-edge noise

The one-third octave sound pressure level is shown in Figure 6 for  $\delta_f = 0^\circ$  with and without the trailing-edge noise  $U_0^5$  scaling law. To focus on the trailing-edge noise, the region of interest encompasses the trailing edge with  $b_g = 0.7$  m and  $c_g = 0.2$  m. The characteristic length scale chosen for the scaling law is the suction side boundary layer displacement thickness  $\delta_1$  at the trailing edge, and the characteristic velocity is the free-stream velocity  $U_0$ . All characteristic values are given for  $\delta_f = 0^\circ$ . Together, they scale the low to medium frequency well.<sup>26</sup> The displacement thicknesses were calculated using XFOIL<sup>22</sup> and are presented in Table 3.

In Figure 6A,C, the sound pressure level decreases with increasing  $\alpha_g$  over a constant  $U_0$ . This observation can be explained by the increase in the boundary-layer thickness and the adverse pressure gradient. For example, the increase of boundary layer thickness from  $\alpha_g = 5^\circ$  to  $7^\circ$  introduces an increase in the sound pressure level by  $10 \log_{10}(\delta_1(\alpha_g = 7^\circ)/\delta_1(\alpha_g = 5^\circ))$  dB and a shift of the spectral level towards the lower frequency by a factor of  $\delta_1(\alpha_g = 5^\circ)/\delta_1(\alpha_g = 7^\circ)$  Hz. Within the dynamic range limitation of the measurement system, the sound pressure level can be partially recovered by normalizing the level accordingly as shown in Figure 6B,D. The normalized sound pressure levels at  $\alpha_g = 5^\circ$  and  $7^\circ$  scale well, whereas at  $\alpha_g = 13^\circ$ , the sound pressure level decays faster for the normalized frequency  $f_c \delta_1 / U_0 > 0.15$ . The increased decay can be attributed to the increased adverse pressure gradient at a large angle of attack on the suction side boundary layer. With strong adverse pressure gradient, the turbulence spectrum level will decrease at higher frequencies when viewed with the outer-scale normalization.<sup>27</sup> The trailing-edge noise sound pressure level is driven by the passage of turbulence across the trailing edge, hence the steeper decay of the sound pressure level from  $\alpha_g = 7^\circ$  to  $\alpha_g = 13^\circ$ .

As a reminder,  $f_c = 5,000$  Hz is dropped in the spectra as described in the previous section. At the high frequency range of  $\alpha_g = 13^\circ$ ,  $f_c > 5,000$  Hz, the spectral level increases for the non-scaled spectra, which is atypical for trailing-edge noise. Hence, to avoid confusion, the scaled spectra of  $\alpha_g = 13^\circ$  are limited to  $f_c \leq 4,000$  Hz.

## 5.4 | Effect of edge noise reduction technologies

The flap side-edge porous substitutes were installed and measured in the same way as a solid flap side-edge to localize the noise source. The region of interest is the same one used when investigating trailing edge scaling. The resulting sound pressure levels for porous flap side-edge, trailing-edge brush, and solid flap side-edge are shown in Figure 7.

### 5.4.1 | Trailing-edge noise

The  $\delta_f = 0^\circ$  configuration in Figure 7A has the porous material affecting only 1/30 of the span length of the model's trailing edge. Hence, the porous material has little effect on the trailing-edge noise reduction. Noise increase was measured for PA120-150 side-edge at  $f_c > 4,000$  Hz because of the increased surface roughness.<sup>28</sup> In contrast, the trailing-edge brush was applied to the full span of the trailing edge. Hence, the porous material's effectiveness for reducing the trailing-edge noise is considerably lower than that of the brush.

The flap-up configuration of  $\delta_f = -5^\circ$  in Figure 7B gradually increases the sound pressure level at higher frequencies compared to the non-deflected flap configuration, whereas the flap-down configuration results in a broadband reduction in sound pressure level. This alteration of the

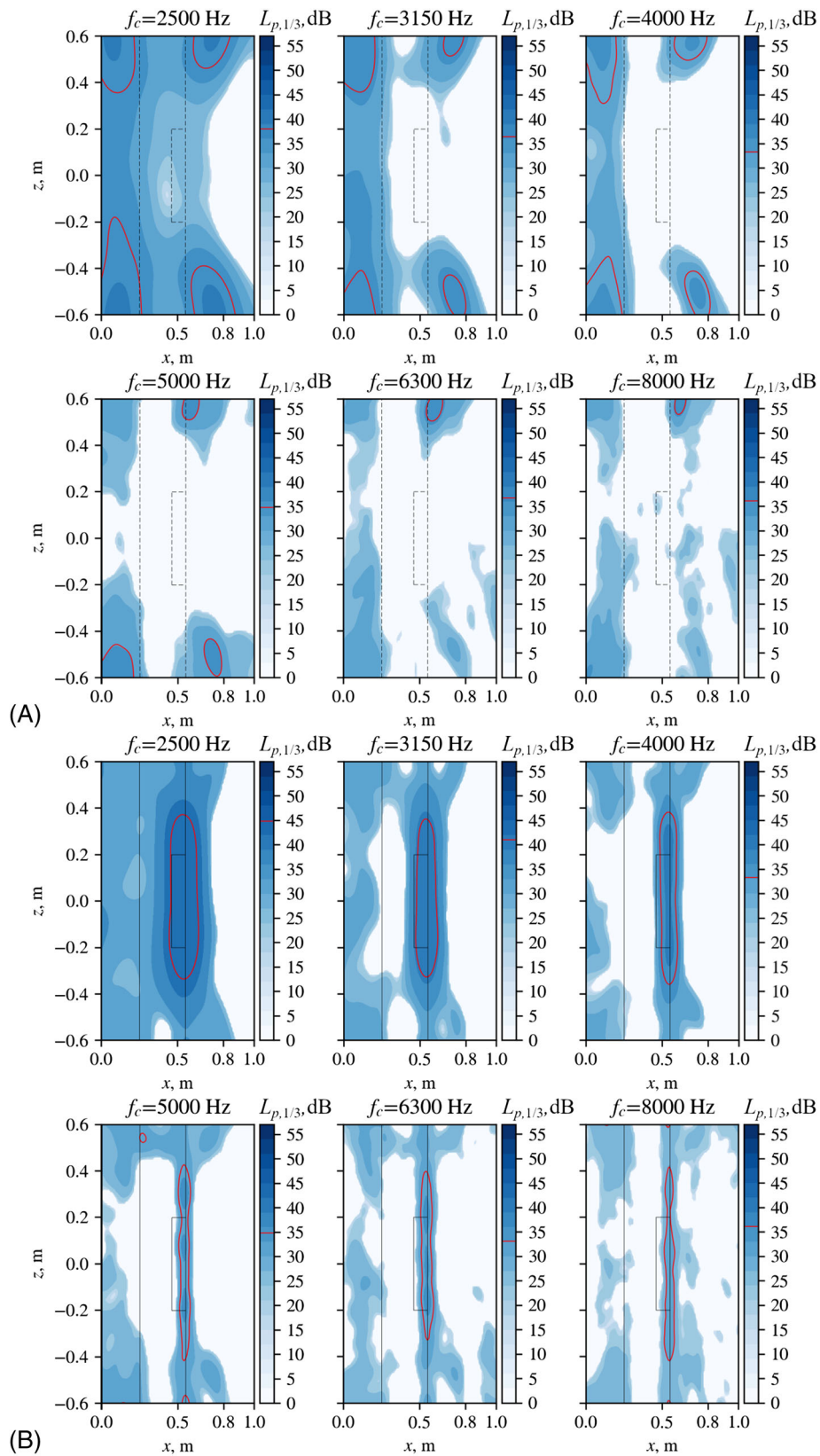


**FIGURE 5** Sound maps with  $U_0 = 50$  m/s (A) exterior noise and (B) trailing-edge noise  $\alpha_g = 5^\circ$  and  $\delta_f = 0^\circ$ . The sound contour where  $\max(L_{p,1/3}) - 3$  dB is highlighted by the red line

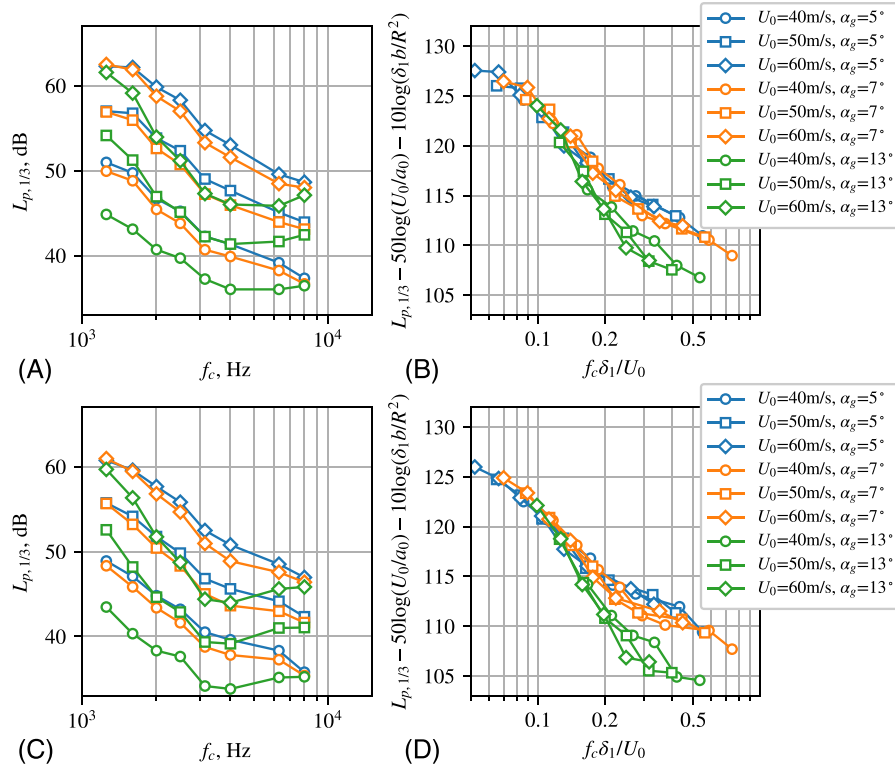


**FIGURE 6** Unscaled (A, C) and scaled (B, D) sound pressure level of trailing-edge noise measured with the phased-microphone array facing the suction-side (A, B) and facing the pressure-side (C, D) of the blade section model

**TABLE 3** Suction side boundary layer displacement thickness  $\delta_1$  computed at the trailing edge

$U_0$ , m/s	$\delta_1/c$		
	$\alpha_g = 5^\circ$	$\alpha_g = 7^\circ$	$\alpha_g = 13^\circ$
40	0.009169	0.012441	0.017808
50	0.008675	0.011728	0.016660
60	0.008299	0.011188	0.015802
150	0.006014	0.008434	0.012626

sound pressure level can be attributed to the local boundary layer's change above the flap's surface. For the  $\pm 5^\circ$  change of flap angle, the sound pressure levels for both porous flap side-edges are similar to those of the solid flap side edge. Similar to the non-deflected flap case, the trailing-edge brush produces a 6 dB reduction in sound pressure level. Hence, for the  $\pm 5^\circ$  flap angle deflection, the flap side-edge noise is not as apparent as the trailing-edge noise in the relevant frequency range.

#### 5.4.2 | Flap side-edge noise

The flap-up configuration  $\delta_f = -10^\circ$  in Figure 7C is fundamentally different than the flap-down one  $\delta_f = 10^\circ$  in Figure 7E. For  $\delta_f = -10^\circ$ , the porous flap side edge does not alter the sound pressure level, whereas for  $\delta_f = 10^\circ$  both porous flap side edges and trailing-edge brush alter the sound pressure level when compared to the solid flap side-edge.

At a glance, it appears that the flap side-edge noise is not relevant for  $\delta_f = -10^\circ$ . However, this outlook could result from the porous material only applied on the flap's side and not on the model's side. The spectra contributed by the narrow strips of the model's trailing edge,  $b_g = 0.2$  m, centered at  $z_c$  are shown in Figure 8, which for brevity shows only the solid flap side-edge and the PA 80-110 flap side-edge. It was confirmed that the sum of sound pressure levels of the narrow sections is equal to the sound pressure level of a region with a span equal to the sum of the span of the narrow sections. Figure 8 classifies three general regions of the model as detailed below:

1. The first region is around the midspan of the model, Figure 8A, where the porous flap side-edge shows little relevance. Changes to the sound pressure level in this figure are related to the value of  $\delta_f$ , which changes the local boundary layer dynamics.

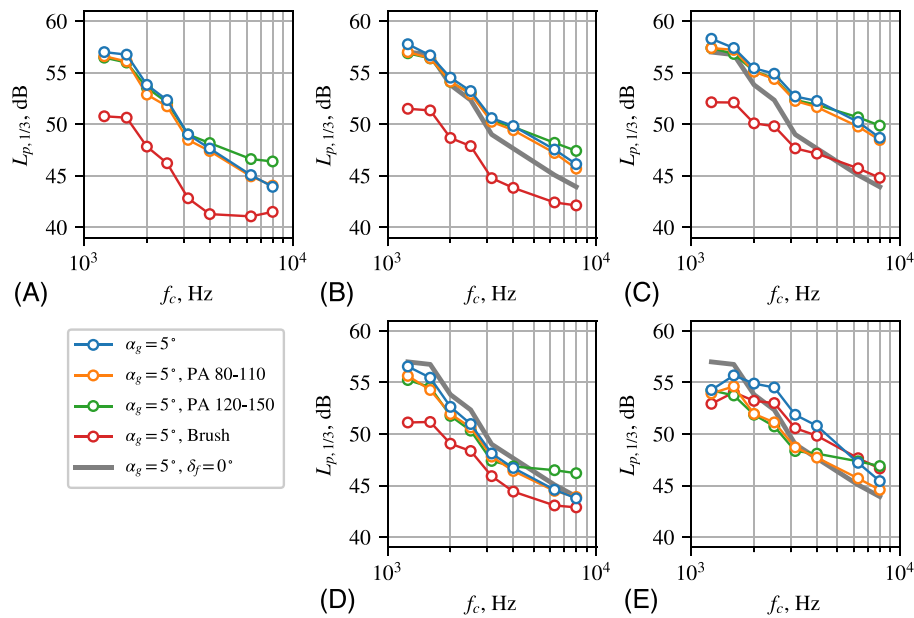


**FIGURE 7** The farfield sound pressure level,  $b_g = 0.7$  m: (A)  $\delta_f = 0^\circ$ , (B)  $\delta_f = -5^\circ$ , (C)  $\delta_f = -10^\circ$ , (D)  $\delta_f = 5^\circ$ , and (E)  $\delta_f = 10^\circ$

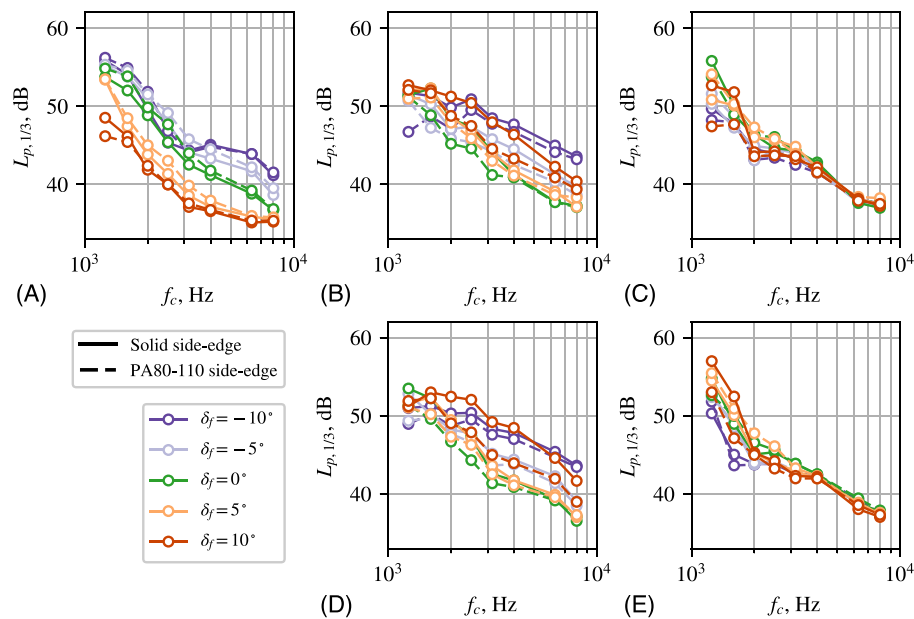


**FIGURE 8** Contributions to the farfield sound pressure level according to the narrow spanwise sections centered at  $z_c$  with  $b_g = 0.2$  m and  $\alpha_g = 5^\circ$ . (A)  $z_c = 0$  m, (B)  $z_c = -0.2$  m, (C)  $z_c = -0.4$  m, (D)  $z_c = 0.2$  m, and (E)  $z_c = 0.4$  m

- The second region encompasses the flap side-edge and shown in Figure 8B,D. The effect of the porous flap-side edge is most notable for  $\delta_f = 10^\circ$  as depicted in Figure 7. The porous flap side edge significantly affects the sound pressure level even for  $\delta_f = 0^\circ$ , because the region processed by CLEAN-SC is a narrow strip focused around the flap side edge.
- The final region is the outboard region shown in Figure 8C,E. The sound pressure levels is affected by  $\delta_f$  for  $f_c < 2,000$  Hz and by  $\alpha_g$  for  $f_c > 2,000$  Hz. The porous side edge affects only the sound pressure level with  $\delta_f = 10^\circ$ .

Comparison of the flap-side edge region, Figure 8B,D, and the outboard region, Figure 8C,E, shows that the solid flap side-edge increases the localized sound pressure level for  $f_c > 2,000$  Hz, and it is observed for  $\delta_f = -10^\circ$  and  $10^\circ$ . However, the porous side-edge is effective in reducing flap side-edge noise only at  $\delta_f = 10^\circ$ . This behavior can be explained by Figure 9 that shows the flap side-edge vortex for (A)  $\delta_f = -5^\circ$  and (B)  $\delta_f = 5^\circ$ . Figure 9A shows that the predominant side-edge vortex develops from the side-edge of the static model, whereas Figure 9B shows that it develops from the flap side-edge. Because the porous material is only installed on the flap side-edge, Figure 9 is a compelling argument that

the porous side-edge is ineffective in reducing flap side-edge noise in the flap-up configuration. The flap deflection angles of the simulated flow field are smaller than those observed in the measurement; however, we believe that the physical phenomenon explained here is retained.

## 6 | DISCUSSION

The IWT-7.5-164 wind turbine's design angle at  $R = 76$  m is  $6^\circ$ , which is achieved in the wind tunnel measurement at approximately  $\alpha_g = 13^\circ$ . However, the blade section model at the flap-down configuration at this angle of attack deflects the flow greatly. Under such conditions, the wake would directly impinge on the flow-collector wall, causing blockage effects and potential structural damage to the wind tunnel. Therefore, the reference angle of attack in the wind tunnel measurement is  $\alpha_g = 7^\circ$  or equivalent to the aerodynamic angle of attack  $\alpha_a$  of  $3^\circ$ .

For the present blade section model with flap, two-dimensional RANS simulations show that a flap deflection of  $5^\circ$  results in a change of lift equivalent to an approximately  $+3^\circ$  change in the aerodynamic angle of attack and vice versa; see Figure 10A. The angle of attack change from

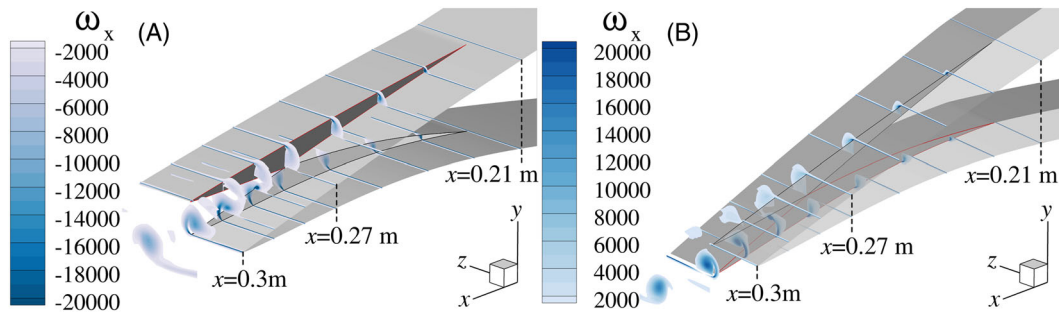


**FIGURE 9**  $k$ - $\omega$  SST simulations of the flap side-edge vortex with  $U_0 = 50$  m/s and  $\alpha_a = 0^\circ$ : (A)  $\delta_f = -5^\circ$  and (B)  $\delta_f = 5^\circ$ . The flap side-edge is demarked by a red line, and the color contour depicts the strength of the chordwise vorticity

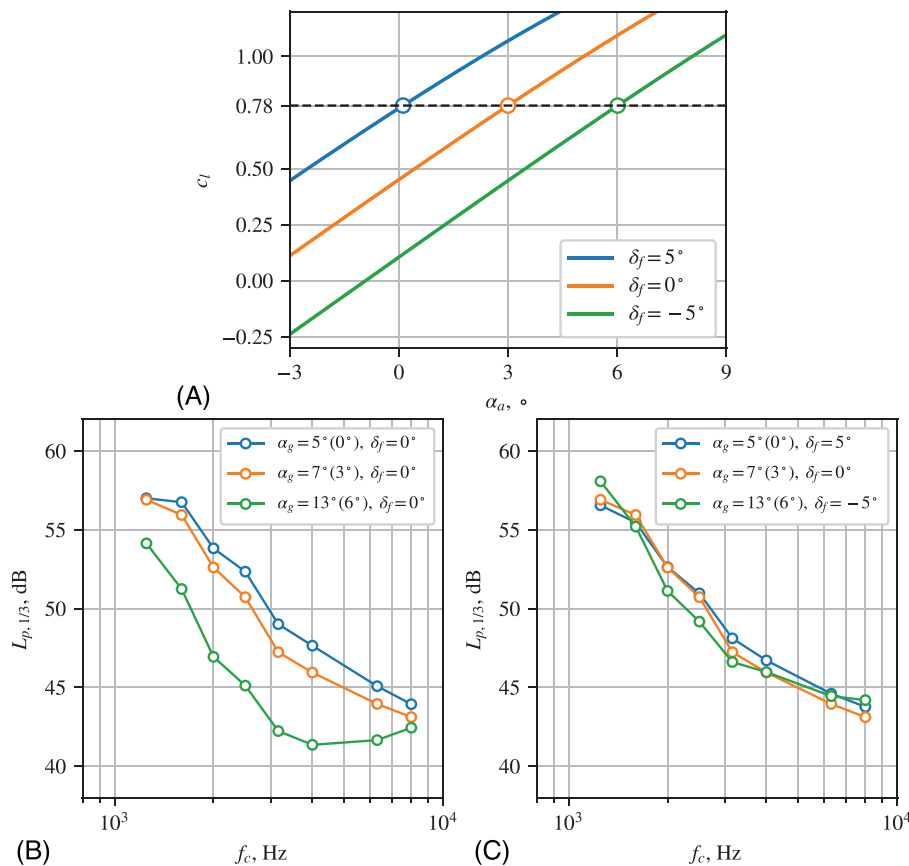


**FIGURE 10** (A) Lift coefficient,  $c_l$  vs. the aerodynamic angle of attack,  $\alpha_a$ , with and without flap deflections from two-dimensional RANS simulations; (B) the one-third octave sound pressure levels without flap deflection and (C) with flap deflection. The value in parentheses indicates the equivalent aerodynamic angle of attack,  $\alpha_a$

the reference is observable in the sound pressure level in Figure 10B due to the change of the boundary layer thickness and pressure gradient, as explained in Section 5.3.

As part of the load control scheme of the rotor blade, load reduction is imparted by a negative flap deflection and load increase by a positive flap deflection. Hence, a reference  $c_l$  at  $\alpha_a = 3^\circ$  can be achieved at  $\alpha_a = 0^\circ$  with a  $5^\circ$  flap deflection and at  $\alpha_a = 6^\circ$  with a  $-5^\circ$  flap deflection. The acoustic effect of the flap deflections is shown in Figure 10C. For the  $5^\circ$  flap deflection, the sound pressure level is reduced in the broadband sense, whereas for the  $-5^\circ$  flap deflection, the sound pressure level is increased, but it has not risen above the reference sound pressure level. Figure 10 demonstrates that, within the measured frequency range, the sound pressure level from a flap deflection between  $\pm 5^\circ$  due to  $\pm 3^\circ$  angle of attack change, does not exceed that of the reference angle of attack.

## 7 | CONCLUSIONS

A small-scale blade section was measured in the Acoustic Wind Tunnel Braunschweig to investigate the acoustic effect of implementing an active trailing-edge. The blade section has a 400 mm span wide and 90 mm chord long flap. Three freestream velocities, three angles of attack, and flap deflection angles between  $-10^\circ$  to  $10^\circ$  were measured using a phased-microphone array. Because of the physical model scale, noise reduction technologies were used to minimize individual sound sources. A trailing-edge brush was implemented at the static and active trailing edge. A narrow part of the flap side edge was substituted with a porous material to reduce the flap side-edge noise and identify the trailing-edge noise.

The measured far-field noise spectra show that the trailing-edge brush performs best at all flap deflection angles, except for the flap deflection angle of  $\delta_f = 10^\circ$ , where porous side-edges are more effective for noise reduction. The sound pressure level of a narrow region around the flap side-edge at  $\delta_f = -10^\circ$  is higher than the rest of the trailing edge for  $f_c > 2,000$  Hz. However, at  $\delta_f = -10^\circ$ , the porous side-edge material does not reduce noise as optimally as at  $\delta_f = 10^\circ$ . A CFD study was conducted to establish the noise mechanism of the two previously mentioned flap deflection angles. It suggests that at large negative  $\delta_f$  the side-edge vortex interacts with the static model's side edge, the edge that was not treated by a porous element, whereas, at large positive  $\delta_f$ , the side-edge vortex interacts with the flap's side-edge that was treated by the porous element. Hence, noise reduction is mitigated for  $\delta_f = -10^\circ$ . It can be concluded from the porous foam and trailing-edge brush study that flap side-edge noise is not a relevant noise source for the small flap deflection angles between  $-5^\circ$  and  $5^\circ$ .

The active trailing-edge is designed to achieve a  $5^\circ$  flap deflection to compensate the change in lift coefficient from a  $-3^\circ$  angle-of-attack change and vice-versa. Both the  $5^\circ$  and  $-5^\circ$  flap deflections as a response from a  $-3^\circ$  and  $3^\circ$  change of the aerodynamic angle of attack, respectively, produce sound pressure levels comparable to the trailing-edge noise of the reference angle of attack,  $\alpha_a = 3^\circ$ , within the measured frequency range.

The findings in this paper are from a small-scale model, based on this a critical limit to the flap deflection angle was established, where above it the flap side-edge noise overtakes the trailing-edge noise. Three Reynolds numbers were investigated in this paper as control of data quality by observing the velocity dependence of the trailing-edge noise; however, this range is not enough to determine a scale relation with the full-scale blade owing to the increased turbulence energy and broader turbulence scales at high Reynolds number flows. Further investigation, numerically or experimentally, should concentrate on the flap side-edge noise of a full-scale blade.

## ACKNOWLEDGEMENTS

The authors' are grateful to Jörn Tychsen (TU Braunschweig) for providing the porous foam materials and to Karl-Stéphane Rossignol (DLR) for his work in calibrating the phased-microphone array. This study, part of the project SmartBlades 2.0, was funded by the German Ministry for Economic Affairs and Energy (BMWi). Open Access funding enabled and organized by Projekt DEAL. WOA Institution: DEUTSCHES ZENTRUM FÜR LUFT UND RAUMFAHRT Consortia Name: Projekt DEAL

## PEER REVIEW

The peer review history for this article is available at <https://publons.com/publon/10.1002/we.2786>.

## DATA AVAILABILITY STATEMENT

The data that support the findings of this study are available from the corresponding author upon reasonable request.

## ORCID

A. Suryadi  <https://orcid.org/0000-0002-5129-5510>

## REFERENCES

1. Popko W, Thomas P, Sevinc A, et al. IWES Wind Turbine IWT-7.5-164. Rev 4. *Technical report*, Bremerhaven, Germany, Fraunhofer Institute for Wind Energy Systems; 2018.
2. Hardin JC. Noise radiation from the side edges of flaps. *AIAA J*. 1980;18(5):549-552.

3. Howe MS. On the generation of side-edge flap noise. *J Sound Vib.* 1982;80(4):555-573.
4. Sen R. Local dynamics and acoustics in a simple 2D model of airfoil lateral-edge noise. In: *Aeroacoustics Conference*; 1996; State College, Pennsylvania. American Institute of Aeronautics and Astronautics.
5. Hardin JC, Martin JE. Flap side-edge noise: acoustic analysis of Sen's model. *AIAA J.* 1997;35(5):810-815.
6. Streett C. Numerical simulation of fluctuations leading to noise in a flap-edge flowfield. In: *36th AIAA Aerospace Sciences Meeting and Exhibit*; 1998; Reno, Nevada. American Institute of Aeronautics and Astronautics.
7. Guo Y. Prediction of flap side edge noise. In: *5th AIAA/CEAS Aeroacoustics Conference and Exhibit*; 1999; Bellevue, Washington. American Institute of Aeronautics and Astronautics.
8. Khorrami MR, Singer BA, Radeztsky RH. Reynolds-averaged Navier-Stokes computations of a flap-side-edge flowfield. *AIAA J.* 1999;37(1):14-22.
9. Brooks TF, Humphreys WM Jr. Flap-edge aeroacoustic measurements and predictions. *J Sound Vib.* 2003;261(1):31-74.
10. Guo Y. On noise reduction by flap side edge fences. *J Sound Vib.* 2004;277(1-2):369-390.
11. Angland D, Zhang X, Moliin N. Measurements of flow around a flap side edge with porous edge treatment. *AIAA J.* 2009;47(7):1660-1671.
12. Murayama M, Yamamoto K, Takaishi T, et al. Airframe noise reduction of flap side-edge using vortex generators. In: *23rd AIAA/CEAS Aeroacoustics Conference*; 2017; Denver, Colorado. American Institute of Aeronautics and Astronautics.
13. Larsen TJ, Madsen HA, Thomsen K. Active load reduction using individual pitch, based on local blade flow measurements. *Wind Energy.* 2005;8(1):67-80.
14. van Dam CP, Berg DE, Johnson SJ. Active load control techniques for wind turbines. *Technical Report.* SAND2008-4809, 943932, Sandia National Laboratory; 2008.
15. Barlas TK, van Kuik GA. Review of state of the art in smart rotor control research for wind turbines. *Prog Aerosp Sci.* 2010;46(1):1-27.
16. Castagnet D, Barlas T, Buhl T, et al. Full-scale test of trailing edge flaps on a Vestas V27 wind turbine: Active load reduction and system identification: Full-scale test of trailing edge flaps on a Vestas V27 wind turbine. *Wind Energy.* 2014;17(4):549-564.
17. Gomez Gonzalez A, Enevoldsen PB, Barlas A, Madsen HA. Field test of an active flap system on a full scale wind turbine. *Wind Energ Sci.* 2021;6(1):33-43.
18. Rossignol KS. Development of an empirical prediction model for flap side-edge noise. In: *16th AIAA/CEAS Aeroacoustics Conference*; 2010; Stockholm, Sweden. American Institute of Aeronautics and Astronautics.
19. Pott-Pollenske M, Delfs J. Enhanced capabilities of the aeroacoustic wind tunnel Braunschweig. In: *14th AIAA/CEAS Aeroacoustics Conference*; 2008; Vancouver, British Columbia, Canada. American Institute of Aeronautics and Astronautics.
20. Rossignol K-S, Delfs J, Boden F. On the relevance of convection effects for a laser-generated sound source. In: *21st AIAA/CEAS Aeroacoustics Conference*; 2015; Dallas, Texas. American Institute of Aeronautics and Astronautics.
21. Sijtsma P. CLEAN Based on spatial source coherence. *Int J Aeroacoustics.* 2007;6(4):357-374.
22. Drela M. XFOIL: An analysis and design system for low Reynolds number airfoils. *Low Reynolds Number Aerodynamics, Lecture Notes in Engineering.* Berlin, Heidelberg: Springer; 1989:1-12.
23. Herr M. Experimental study on noise reduction through trailing edge brushes. *New Results in Numerical and Experimental Fluid Mechanics V.* Berlin, Heidelberg: Springer Berlin Heidelberg; 2006:365-372.
24. Herr M, Rossignol K-S, Delfs J, Lippitz N, Mößner M. Specification of porous materials for low-noise trailing-edge applications. In: *20th AIAA/CEAS Aeroacoustics Conference*; 2014; Atlanta, GA. American Institute of Aeronautics and Astronautics.
25. Rossignol K-S, Rossian L, Suryadi A, Herr M, Ewert R, Delfs J. Effect of porous materials on the acoustic emissions of a circulation-control high-lift airfoil. In: *DAGA 2020 - 46 Jahrestagung für Akustik*; 2020:4.
26. Goody M. Empirical spectral model of surface pressure fluctuations. *AIAA J.* 2004;42(9):1788-1794.
27. Nan Hu. Empirical model of wall pressure spectra in adverse pressure gradients. *AIAA J.* 2018;56(9):3491-3506.
28. Rossignol K-S, Suryadi A, Herr M, Schmidt J, Tychsen J. Experimental investigation of porous materials for trailing-edge noise reduction. *Int J Aeroacoustics.* 2020;19(6-8):365-384.

**How to cite this article:** Suryadi A, Jätz C, Seume JR, Herr M. Identifying the flap side-edge noise contribution of a wind turbine blade section with an adaptive trailing edge. *Wind Energy.* 2022;1-12. doi:[10.1002/we.2786](https://doi.org/10.1002/we.2786)